

Unraveling the Origin and Mechanism of Nanofilament Formation in Polycrystalline SrTiO₃ Resistive Switching Memories

Deok-Hwang Kwon, Shinbuhm Lee, Chan Soon Kang, Yong Seok Choi, Sung Jin Kang, Hae Lim Cho, Woonbae Sohn, Janghyun Jo, Seung-Yong Lee, Kyu Hwan Oh, Tae Won Noh, Roger A. De Souza, Manfred Martin,* and Miyoung Kim*

Three central themes in the study of the phenomenon of resistive switching are the nature of the conducting phase, why it forms, and how it forms. In this study, the answers to all three questions are provided by performing switching experiments in situ in a transmission electron microscope on thin films of the model system polycrystalline SrTiO₃. On the basis of high-resolution transmission electron microscopy, electron-energy-loss spectroscopy and in situ current–voltage measurements, the conducting phase is identified to be SrTi₁₁O₂₀. This phase is only observed at specific grain boundaries, and a Ruddlesden–Popper phase, Sr₃Ti₂O₇, is typically observed adjacent to the conducting phase. These results allow not only the proposal that filament formation in this system has a thermodynamic origin—it is driven by electrochemical polarization and the local oxygen activity in the film decreasing below a critical value—but also the deduction of a phase diagram for strongly reduced SrTiO₃. Furthermore, why many conducting filaments are nucleated at one electrode but only one filament wins the race to the opposite electrode is also explained. The work thus provides detailed insights into the origin and mechanisms of filament generation and rupture.


emerging applications, particularly for the development of non-volatile memory devices and new logic devices as well as neuro-electronics.^[4–6] For metal/insulator/metal (MIM) devices, three different switching mechanisms have been identified in the literature: the filamentary mechanism is based on the formation of a highly conductive filament during an initial forming process^[1,2]; the interfacial mechanism is based on modification of the interfacial resistance between the insulator and the metal electrode^[2,3]; and the third type of switching mechanism is due to homogeneous polarization and switching of the complete bulk of the insulator and needs no forming process.^[7,8] While filamentary switching is by far the most frequently found case, the filament has been clearly identified only in few cases in anion-based switching systems,^[9,10] compared to cation-based switching systems.^[11–16] The nature of the conducting path and its redox process in anion-based switching system has

The hysteretic behavior of the resistance as a function of an external bias has been observed in a range of dielectric materials.^[1–4] Specifically, resistive-switching phenomena in redox-based systems have attracted growing interest because of the possibilities for

been remained ambiguous, despite a thorough understanding of resistive switching being essential for controlling the properties of resistive-switching devices, and ultimately, for the design of future resistive-switching systems.

Dr. D.-H. Kwon,^[†] Dr. C. S. Kang, Dr. Y. S. Choi, Dr. S. J. Kang, H. L. Cho, Dr. W. Sohn, Dr. J. Jo, Dr. S.-Y. Lee, Prof. K. H. Oh, Prof. M. Martin, Prof. M. Kim
Department of Materials Science and Engineering
Seoul National University
Seoul 08826, Republic of Korea
E-mail: mkim@snu.ac.kr

Dr. D.-H. Kwon,^[†] Dr. C. S. Kang, Dr. Y. S. Choi, Dr. S. J. Kang, H. L. Cho, Dr. W. Sohn, Dr. J. Jo, Dr. S.-Y. Lee, Prof. K. H. Oh, Prof. M. Kim
Research Institute of Advanced Materials
Seoul National University
Seoul 08826, Republic of Korea

 The ORCID identification number(s) for the author(s) of this article can be found under <https://doi.org/10.1002/adma.201901322>.

^[†]Present address: Department of Materials Science and Engineering, University of California, Berkeley, CA 94720, USA

Prof. S. Lee
Department of Emerging Materials Science
Daegu-Gyeongbuk Institute of Science and Technology
Daegu 42988, Republic of Korea

Prof. S. Lee, Prof. T. W. Noh
Department of Physics and Astronomy
Seoul National University
Seoul 08826, Republic of Korea

Prof. T. W. Noh, Prof. M. Kim
Center for Correlated Electron Systems
Institute for Basic Science (IBS)
Seoul 08826, Republic of Korea

Prof. R. A. De Souza, Prof. M. Martin
Institute of Physical Chemistry
RWTH Aachen University
Aachen 52074, Germany
E-mail: martin@rwth-aachen.de

DOI: 10.1002/adma.201901322

Here, we elucidate the mechanism of filament formation and its associated resistive switching in SrTiO_3 (STO) by proposing a phase diagram based on experimentally observed microstructural and chemical information near the conducting paths. STO is one of the most extensively studied perovskite materials and exhibits many intriguing physical and chemical properties. In particular, its electrical properties range from superconducting to insulating depending on the type and concentration of intrinsic or extrinsic defects.^[17,18] Moreover, the defect chemistry in STO, as a model material for perovskite oxides, has long been a subject of extensive studies, and knowledge of point-defect behavior and solid state reactions in STO is at a rather advanced stage.^[19–22] The mobilities of anions and cations and their corresponding point defects in the bulk and also in the vicinity of extended defects, such as dislocations or grain boundaries (GBs)—indispensable knowledge for understanding the atomistic origin of the resistive switching introduced by ionic transport—can be predicted quantitatively in STO from references.^[20,23]

Mostly, oxygen vacancies are believed to play a central role in resistive switching in STO, although it is worth noting that the possibility of an active role of Sr-vacancies has also been evoked intermittently.^[24,25] Consequently, an investigation of the microstructural evolution in polycrystalline STO during the switching process is expected to provide fundamental and valuable information about the switching mechanism in dielectrics.

Here, we employ in situ I - V measurements in a transmission electron microscope (TEM) to identify the highly conducting crystal phase, which appeared and partially ruptured after the FORMING (or SET) and RESET operations, in resistive-switching STO. Complete rupture was also observed depending on RESET operation. (see filament rupture section) Previously, the in situ TEM approach was successfully employed for the first direct verification of the filamentary switching model of resistive switching in the TiO_2 system.^[9] Recently, the in situ I - V /TEM approach has been applied to other ReRAM systems as well to reveal the nature of the conducting filaments, particularly in conducting-bridge RAM^[13–15,26–29] or in other bipolar switching systems.^[30–33] However, it has been rarely employed for the study of unipolar oxide systems, partly because of the complexities in phase identification.^[10] The approach permits filamentary structures and/or their local compositions in the matrix of a cross-sectional TEM sample to be probed by acquiring images, spectra, and I - V curves of the local structure simultaneously. In the present study, by applying these powerful techniques to STO, we found that the highly conductive filament in STO consists of the Ti-rich phase $\text{SrTi}_{11}\text{O}_{20}$. Moreover, the metallic nature of the observed filament, $\text{SrTi}_{11}\text{O}_{20}$,^[34] was further verified by electron energy loss spectroscopy (EELS) and density functional theory (DFT) calculations. Structural investigation of the filament imparted two important findings: remarkably, filaments were only generated at specific GBs, as revealed from the crystallographic orientation relationships between the neighboring STO grains. Moreover, both O and Sr defects played a decisive role in the generation of the filaments, as evidenced by the presence of a Ruddlesden–Popper (RP) phase, $\text{Sr}_3\text{Ti}_2\text{O}_7$, in the vicinity of the $\text{SrTi}_{11}\text{O}_{20}$ filament. These new findings, together with the kinetic switching behavior, lead to an in-depth understanding of the origin of resistive switching in STO. On this basis, we propose a new thermodynamic phase diagram that quantitatively demonstrates how phase transformation

between the insulating and metallic phases takes place when STO near the GBs is electrochemically polarized by an external voltage. This work provides comprehensive insight into a new way of controlling the filament density, position, size, and current individually by structural design of implementing specific GBs, which has been a major challenge in resistive-switching devices.

In Situ FORMING Process and Identification of the Conducting Phase: In situ FORMING (or SET) processes were carried out to generate filaments in the TEM specimens. Cross-sectional TEM samples were prepared by focused ion beam (FIB) milling of cells in the ON state; however, this method did not ensure that the TEM samples were also in the ON state and featured conducting pathways. In fact, most TEM samples were in the high-resistance state and were SET inside the TEM by applying an appropriate bias (with currents below the compliance current) to an in situ I - V /TEM holder. Note that, initially, the pristine STO film was polycrystalline SrTiO_3 (Figure S1, Supporting Information), high resistance state where the leakage current is as low as nA (<0.1 V) within $10\text{--}100\text{ }\mu\text{m}^2$ device cell.^[35,36] Specifically, a bias was applied to the bottom electrode (BE), while a Pt/Ir-coated W scanning tunneling microscope (STM) tip, held in contact with the top electrode (TE) of the sample, was grounded. To inhibit direct current flow through the TE to the Cu grid, the TE near the grid was cut using an FIB, as shown in Figure 1a. For consistency, all experiments

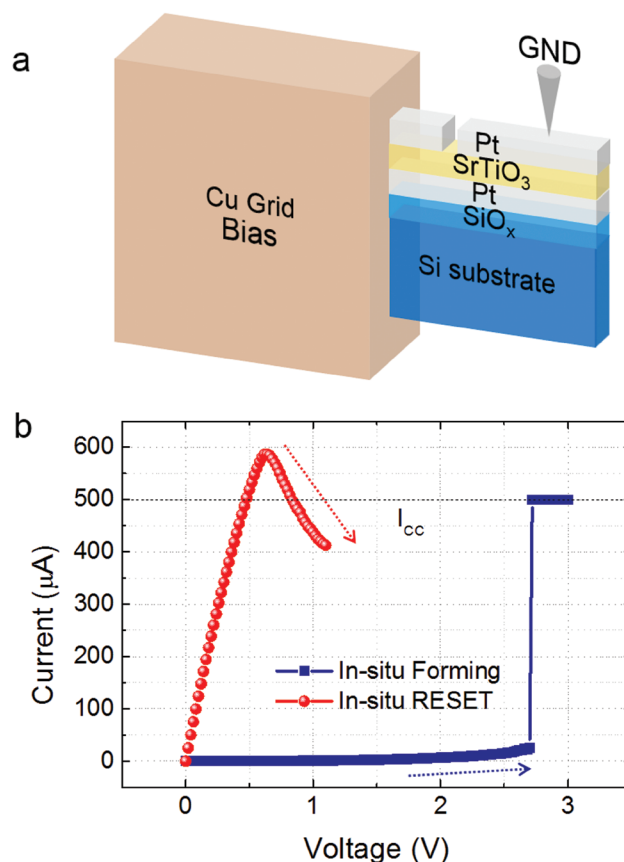


Figure 1. Schematic of the TEM sample use in the in situ I - V experiments and the corresponding I - V curves of in-situ FORMING and RESET. a) Schematic of the Pt/ SrTiO_3 /Pt TEM sample. b) I - V curves of the in situ FORMING (blue squares) and RESET (red circles) process of the TEM sample.

were performed with the TE connected to ground and the BE biased. An example of I - V curve, with in situ Forming and RESET, is given in Figure 1b. (Corresponding images after filament formation and rupture are shown in Figure 2.) As is seen in Figure 1b, the I - V curve shows unipolar switching. Details about the switching properties of cells have been previously reported.^[35,36] Note that the Forming process was carried out through multiple I - V sweeps by increasing compliance current step by step (Figure S2a, Supporting Information) to prevent significant heat generation and damage to the sample. The experimental conditions during the FORMING (or SET) and RESET processes are described in the Supporting Information.

Following the in situ FORMING process, the STO layer was scanned and probed using the Pt/Ir-coated W tip while reading the current to locate conducting channels applying constant voltage (<0.1). (Figure S3, Supporting Information) The contact area of the tip was nominally ≈ 20 nm in diameter. A few 5–30 nm wide conducting channels were detected in each 3–4- μ m-wide sample in the strongly formed TEM specimens. We found that the density of filaments did not vary with the forming current (compliance current); however, the current in a single filament varied from -5 to -125 μ A depending on the compliance current at an applied bias of -0.1 V (see Figure S2b, Supporting Information). The current in the matrix was <1 nA, whereas it was >100 nA near the filament, where the magnitude of the current within and around the filaments depended on the FORMING conditions. From these results, the conductivities in the matrix, specific GBs, and the filaments were estimated. These data are listed in Table 1, and these results were consistently reproduced in other TEM specimens.

The conducting area identified by the in situ I - V measurements was investigated with high-resolution (HR) TEM images and EELS. Importantly, a secondary phase, $\text{SrTi}_{11}\text{O}_{20}$ ^[34] (shaded by the red colors in Figure 2a), was identified in the conducting area. The filament structures had many distinctive diffraction peaks with d -spacings larger than 3.91 and 3.88 Å, which correspond to the largest spacings of STO and other perovskite type RP phases, respectively. These d -values indicate the possibility of $\text{Sr}_2\text{Ti}_6\text{O}_{13}$ ^[37] and $\text{SrTi}_{11}\text{O}_{20}$ ^[38] phases, which have larger lattice parameters than STO. The crystalline structure was tilted into a specific orientation to obtain clear diffraction peaks, with spacings larger than 3.9 Å to discriminate the normal STO structures from others.

Figure 2a shows an HRTEM image of one of the conducting areas. Fast Fourier transforms (FFTs) of the HRTEM images from the corresponding area (see Figure 2e) coincide well with the simulated FFT data for $\text{SrTi}_{11}\text{O}_{20}$, as shown in Figure 2g. Filament structure, $\text{SrTi}_{11}\text{O}_{20}$ is connected thorough BE to TE (clear contact is shown in Figure S4, Supporting Information). Interestingly, RP phases near the filaments (shaded by the green color in Figure 2a) were commonly observed (a further example is shown in Figure S5, Supporting Information). Each FFT from the area numbered one and two in Figure 2a (marked

by white dotted box) is shown in Figure 2b,e. Figure 2b is consistent to superposition of diffraction patterns of STO matrix (yellow circle) and RP phase (green circle) as indexed in Figure 2c,d. Figure 2e is also consistent to superposition of diffraction patterns of STO matrix (yellow circle) and filament (red circle) as indexed in Figure 2f,g. Color code red, yellow, and green correspond to filament, STO matrix, and RP phase, respectively. Note that (011) peak marked in Figure 2g corresponds to 6.4 Å [also marked (011) plane in Figure 2a], which is not arguable with STO or RP phase as described above. Further detailed analysis of crystallographic orientation will be discussed in the Microstructure analysis section. (Analyses of other cases, different regions and different orientations are included in the Supporting Information.) It is worth noting that the $\text{SrTi}_{11}\text{O}_{20}$ structure is a SrO-deficient phase (i.e., TiO_2 -rich) compared with STO, whereas RP is SrO-rich (i.e., TiO_2 -deficient), which suggests that filament formation in unipolar switching STO is caused by a decomposition of STO into a Ti- and an Sr-rich phase.

The possibility of double diffraction from two overlapping grains, which is often misinterpreted as a presence of another phase, was further examined using EELS measurements in a scanning TEM (STEM) mode. The EELS edge of the filaments of the highly conducting area was compared with that of the matrix. We observed that the shape of the EELS edge of the filament differed significantly from that of the STO matrix (see Figure 3a) as well as from the oxygen-deficient STO_{3-x} .^[38] Figure 3b shows Ti L edges of a conducting phase (hereafter referred to as the filament) and the neighboring matrix. Both the Ti L_3 and L_2 edges from the filament exhibited substantially reduced e_g states and weakened crystal-field splitting compared with the matrix. Moreover, the L_3/L_2 ratio for the filament structure, which has been interpreted as an indication of the oxidation states of transition metals,^[39] was larger than the L_3/L_2 ratio in the matrix, implying that the oxidation state of Ti was lower in the filament than in the matrix.

The O K edges in the filament also exhibited a distinctive structure, which differed from those of normal STO and O-deficient STO.^[38] Figure 3c shows a representative O K edge of a filament, revealing suppression of the first peak, indicative of an enhancement in the hybridization of π -bonding between O 2p and Ti 3d orbitals.^[40] Furthermore, by comparing the intensities of the O spectra relative to the normalized Ti continuum, we observed that the O fraction in the filament structure was smaller than that in the matrix.^[41] Figure 3a clearly shows that the intensity of the O continuum in the filament is lower than that in the STO matrix (see Figure S6, Supporting Information). Evidently, both the Ti and O edges strongly suggest the presence of a phase that is not STO. Note that, EELS were able to be acquired across the center of filament structure (a few to 10 nm) angle independently (grain orientation), which indicates that these features are not from GB/dislocation. (see Figure S7, Supporting Information) These results are in good agreement with the EELS simulations for $\text{SrTi}_{11}\text{O}_{20}$ using first-principles DFT calculations. (Figure 3d) The total density of states of the $\text{SrTi}_{11}\text{O}_{20}$ structure reveals that it is metallic, with the Fermi energy in the conduction band (see Figure S8, Supporting Information). Recently, this $\text{SrTi}_{11}\text{O}_{20}$ phase was suggested as a filament structure in

Table 1. Estimated conductivity of the nanofilament and its neighbors.

| Element | Matrix | Specific grain boundary | $\text{SrTi}_{11}\text{O}_{20}$ |
|---|-------------------|-------------------------|---------------------------------|
| Conductivity [$\Omega^{-1} \text{ m}^{-1}$] | $\approx 10^{-3}$ | $\approx 10^2$ | $\approx 10^5$ |

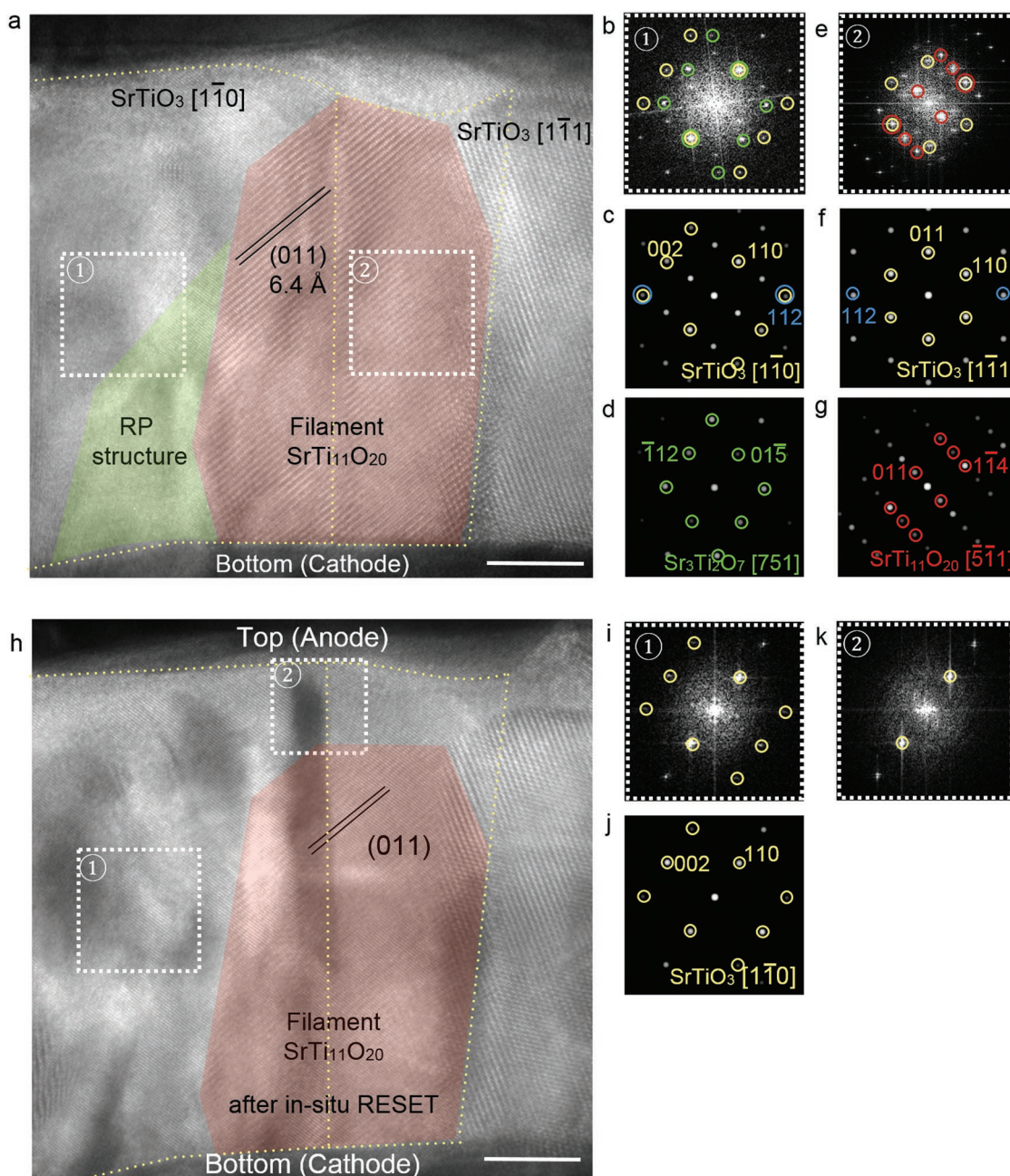


Figure 2. Atomic structure of the filament and neighboring matrix from the On and Off states. a) An HRTEM image of the sample, including a filament and the surrounding matrix after in situ FORMING. b,e) FFTs from the area marked by the white squares, numbered one and two, in (a). c,d) FFT simulations of the SrTiO_3 and $\text{Sr}_3\text{Ti}_2\text{O}_7$ shown in (b). f,g) FFT simulations of the SrTiO_3 and $\text{SrTi}_{11}\text{O}_{20}$ shown in (e). h) An HRTEM image of the identical filament in (a) after in situ RESET. i,k) FFTs from the area marked by the white squares, numbered one and two, in (h). j) FFT simulation of SrTiO_3 (scale bar: 10 nm).

$\text{STO}^{[42]}$ by TEM and electrical measurements and confirmed subsequently.^[43]

Filament Rupture (in situ RESET): The physical properties of the $\text{SrTi}_{11}\text{O}_{20}$ phase were further studied by examining the structure after the RESET process (i.e., the rupture of filaments). The filaments ruptured either completely or partially, depending on whether the current was greater or smaller than ≈ 1 mA. Following rupture, the crystal structure of the transformed regions of the filaments became STO again, as determined by both HRTEM and EELS analyses. This clearly

demonstrates $\text{SrTi}_{11}\text{O}_{20}$ phase is the filament structure in the STO system.

Figure 1b shows I - V curves corresponding to partial filament rupture following the application of a moderate current (< 1 mA) (For complete filament rupture see Figure S9, Supporting Information). With conical filaments (truncated conical shape), the section of the filament close to the anode was ruptured. Figure 2h shows the same filament shown in Figure 2a after in situ RESET. As it is seen, filament (shaded by the red color) near the TE is ruptured (Figure 2h).

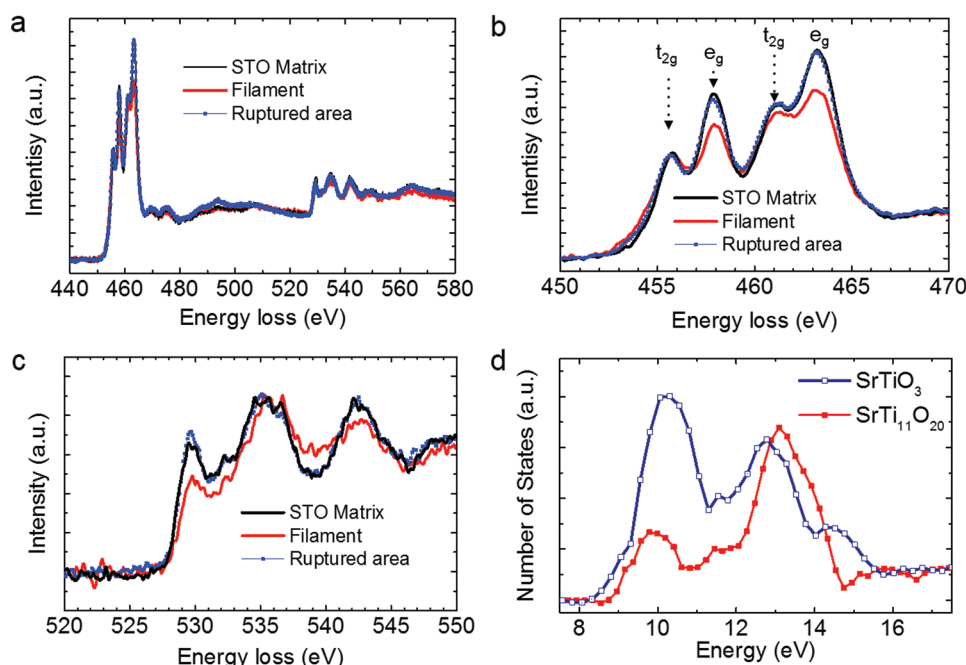


Figure 3. EELS of filament structures and the matrix. a) EELS data for the Ti L edge and O K edge of the filament (red line), STO matrix (black line), and ruptured area of filament (blue line with rectangle symbol). b) Enlarged plot of Ti L edge. The e_g states of each L_3 and L_2 edge decreased significantly in the filament compared to STO matrix. c) Enlarged plot of the O K edge. The first peak of the three features was suppressed in the filament. After in situ RESET, ruptured area of filament recovers to STO EELS in both Ti L and O K edge. d) Projected density of states O K edges calculated from SrTiO₃ and SrTi₁₁O₂₀ using DFT.

Diffraction peaks corresponding to filament structure (Figure 2g) and RP structure (Figure 2d) both disappeared as shown in Figure 2k,i, respectively. EEL spectra of both the Ti L and O K edges were consistent with normal STO following filament rupture, suggesting that the filament and the adjacent RP phase were transformed back to STO. The crystal-field splitting of t_{2g} and e_g re-appeared, and the intensity of e_g recovered (see Figure 3).

For cylindrical filaments, complete rupture occurred gradually from the center. This observation is consistent with the expectation that the middle part of the filament would rupture with a cylindrical geometry^[44] because both sides of the filament are well connected with the electrodes and hence have heat dissipation routes, resulting in a higher temperature at the center of the filament. This explanation suggests that Joule heating caused by a high electrical current plays a major role in the rupture process.

As a consequence of the above observations during the RESET process, Sr and O have to be redistributed again, i.e., the Sr-rich RP-phase must now provide Sr and O to the Ti-rich filament to recover the parent perovskite phase, STO.

Microstructures near the Filaments: The TEM analyses showed that resistance switching from the high-resistance state to the low-resistance state is associated with the formation of a secondary, metallic phase. We further investigated the distribution of filaments and the microstructural origin of filament generation in the polycrystalline STO thin films by examining the locations and crystal orientations where filaments were generated. We found that filaments were only generated at specific types of boundaries.

Electron diffraction showed that the polycrystalline STO thin film exhibited a preferential growth of the (011) plane on the (111)-dominant Pt electrode, while some grains had the (111) growth plane, probably because of little lattice mismatch with the Pt (111) electrode.^[45] Because of the columnar growth of STO, the GBs were connected with both the TE and BE. Extensive data analysis showed that most filaments were located between these two grains, particularly at the GBs where two (112) planes were twisted by 90°, or where (112) and (110) planes met. As shown in Figure 2c,f, grains of both the (111) and the (011) growth planes exhibited {112} peaks at the same position in the horizontal direction (indicated by blue circles), where two {112} planes were rotated by 90°. These structural features provide information on nucleation sites for the formation of filaments. More than 70% of the filaments were generated at GBs where (112) planes were twisted by 90°, and the remainder were generated where (112) and (110) planes met. We did not observe any other cases in many TEM samples of more than 30 filaments. Figures S10 and S11 in the Supporting Information list some examples. As a summary, **Figure 4** shows a schematic of the orientations of the matrix, filament, and RP structure.

The initial nucleation process of the filaments may be inferred from the locations at which they were generated. Interestingly, the STO (112) and (110) planes have slabs consisting of oxygen ions only. Both the (112) and (110) planes are composed of [SrTiO]⁴⁺ and [O₂]⁴⁻ layers, as shown in Figure S11 in the Supporting Information. Notably, these specific GBs are highly unstable as revealed by density functional calculations (Figure S12, Supporting Information). Note that the FORMING

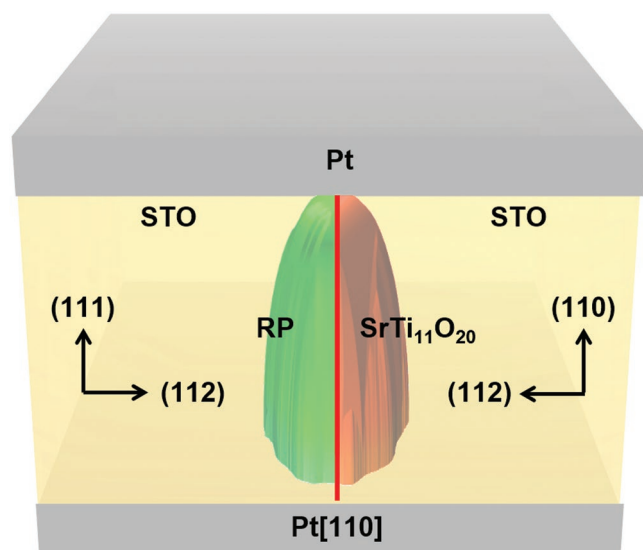


Figure 4. Schematic of the geometric relations between the filament and matrix. The filaments preferentially formed at 90° twisted (112) GBs between (111) and (011) grains that meet in the (112) plane. –RP phase structures are shown adjacent to the filaments, as commonly observed in the HRTEM images. GB is illustrated by the red line.

process required relatively large initial currents ($>30 \mu\text{A}$ at -6 V), agreeing with several reports which noted the importance of the pre-existence of high leakage pathways such as dislocations at pristine state in single-crystal ReRAM systems.^[46–49]

These results present two important findings. First, unipolar switching in polycrystalline STO is associated with the formation of the secondary phases $\text{SrTi}_{11}\text{O}_{20}$ (Ti-rich, metallic filament) and $\text{Sr}_3\text{Ti}_2\text{O}_7$ (Sr-rich RP structure, insulator^[50]). In contrast to many previous models and experimental results suggesting that dislocations in the STO system form filament channels,^[2,46,47] we show that crystalline structures with a size in the range 10–20 nm and which exhibit metallic behavior are responsible for resistive switching. Second, filaments were generated only at specific GBs, as revealed from relationships between the orientation of the filaments and that of the neighboring STO grains. Moreover, the Ti-rich filament is accompanied by a neighboring Sr-rich RP phase, indicating that redistribution of Sr and O plays also a major role during filament formation. Estimates of the electrical conductivity of the each phase (i.e., the matrix, specific GBs, and $\text{SrTi}_{11}\text{O}_{20}$) are listed in Table 1, and details of the calculations are provided in the Supporting Information (see approximate conductivity estimation).

In this section, we present a model that explains the formation of the experimentally observed conductive filament during resistive switching of SrTiO_3 and its rupture as well. Deriving an explanation for the recurrent structural and/or compositional transition between insulating and metallic phase by an external bias with the same polarity (unipolar switching) is highly challenging. One common explanation is a combination of Fickian diffusion driven by a concentration gradient and Soret diffusion driven by a temperature gradient, as proposed by Williams et al.^[51] The primary assumption of this model is that oxygen vacancies move up the temperature gradient generated by Joule

heating. The resulting compositional variations lead to the formation of a new phase. This model, however, still vaguely describes the initial formation of the filaments that lead to the temperature gradient for the SET process. More importantly, this is much more complicated in the case of ternary systems, such as STO with the possibility of three mobile ions.

Here, we propose electrochemical polarization due to the external bias and the resulting variation of the oxygen activity across the sample as the origin of the resistive switching. Our experiments have shown that filament formation is connected to the presence of GBs in STO (see Figure 2). It is well known that the GB core in STO is positively charged resulting in adjacent space charge layers (SCL) with depletion of oxygen vacancies, $\text{V}_\text{O}^{\bullet\bullet}$, and enrichment of electrons, e' .^[49,52] As the STO film that is used for resistive switching is very thin (typical thickness less than 100 nm), we consider in our model only a single GB across the film, as shown schematically in Figure 5a. The GB core is positively charged, while the SCL is negatively charged. The adjacent bulk is charge neutral, $2[\text{V}_\text{O}^{\bullet\bullet}] = [\text{Ac}'] + [e']$. Here, we allow for (unintentional) doping with an acceptor Ac' . In Figure 5a, the shown concentration profiles depict the concentration profiles of oxygen vacancies and electrons perpendicular to the GB. As Figure 5a corresponds to the unpolarized state, i.e., prior to applying an external voltage, there are no concentration gradients in the direction parallel to the GB. Figure 5b shows the resulting partial conductivity profiles for oxygen vacancies, σ_v , and electrons, σ_e , in STO at room temperature (note the logscale for the conductivities). For both plots, we have used literature values for the driving energy for space-charge formation at a GB in $\text{STO}^{[52]}$ and the mobilities of oxygen vacancies and electrons.^[20,53]

Applying now at room temperature an external voltage between the TE and BE, i.e., parallel to the GB, results in an electric current I across the film that is mainly confined to the SCL and carried initially by electrons only. Due to Joule heating the temperature of the inner part of the SCL will increase (Figure 5c). With increasing temperature, eventually also the mobility of the oxygen vacancies within the hot zone will increase. However, due to the combination of the depletion profile and the temperature profile the flux of oxygen vacancies parallel to the GB will be confined to the outer part of the SCL (see Figure 5d). Driven by the external voltage, the oxygen vacancies will drift parallel to the GB from the TE towards the BE resulting in a depletion of V_O near the TE and enrichment of V_O near the BE. Here, we assume that both the TE and the BE completely block the flux of oxygen (vacancies). In other words, the initially homogeneous oxygen vacancy fraction of STO across the film (see dashed line in Figure 5e) becomes inhomogeneous (solid line in Figure 5e) due to electrochemical polarization. Near the TE STO becomes nearly stoichiometric, corresponding to a rather high oxygen activity, $a_\text{O}_2(\text{TE})$, while near the BE STO becomes highly non-stoichiometric, $\text{SrTiO}_{3-\delta(\text{BE})}$, corresponding to a rather low oxygen activity, $a_\text{O}_2(\text{BE})$ (It must be emphasized that the STO film outside the hot zone remains (nearly) homogeneous despite the applied voltage, as the oxygen vacancies in the colder part of the film are much less mobile than in the hot part.).

The ratio of the oxygen activities at the BE and at the TE, $a_\text{O}_2(\text{BE})/a_\text{O}_2(\text{TE})$, can be estimated assuming “full

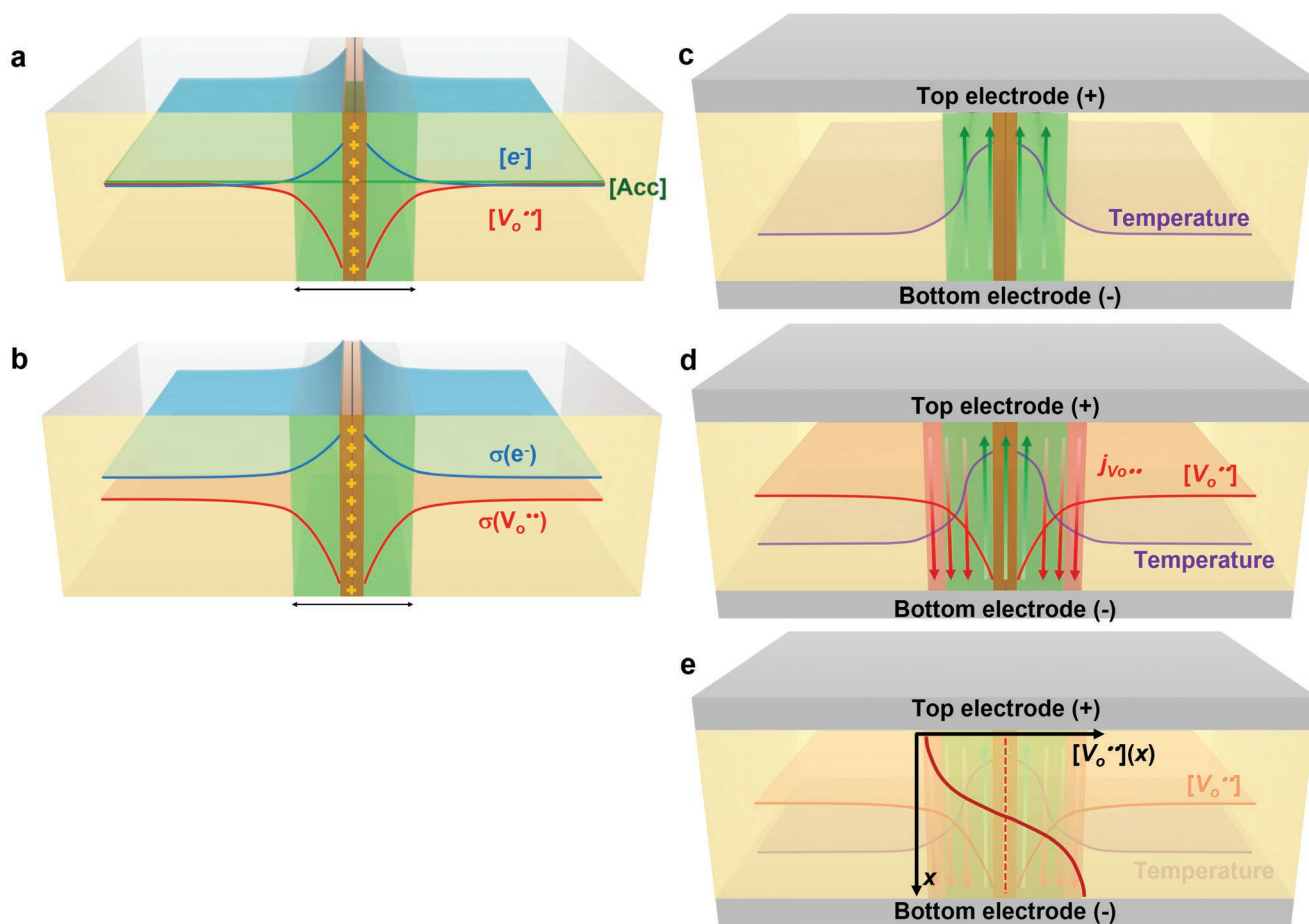


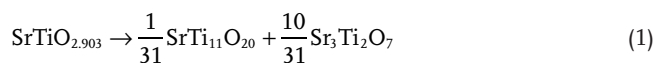
Figure 5. Modeling of GB in initial stage of filament formation. a) Two STO grains separated by a positively charged GB core (++++) and adjacent SCL with depletion of oxygen vacancies and enrichment of electrons (log scale). b) Partial conductivity profiles of oxygen vacancies, σ_{V_o} , and electrons, σ_e (log scale). c) Schematic presentation of the initial state after applying a voltage between BE and TE, showing that the electronic current (green arrows) is confined to the SCL. d) Due to Joule heating the temperature around the center of the SCL increases and oxygen vacancies become mobile and drift towards the BE. e) Oxygen vacancy profile across the film in the polarized state

polarization”, in which the flux of oxygen vacancies (or oxygen ions), $j(V) = -j(O^{2-}) = L_{OO} \cdot d\eta(O^{2-})/dx$, is zero (L_{OO} is the transport coefficient and $\eta(O^{2-})$ the electrochemical potential of oxygen ions). In this steady state, with zero $j(V)$ and non-zero L_{OO} , the driving force $d\eta(O^{2-})/dx$ must be zero, from which we obtain $aO_2(\text{BE})/aO_2(\text{TE}) = \exp(-4FV/RT)$ (here F is the Faraday constant, V the applied voltage, R the gas constant, and T the absolute temperature. The results are shown in Figure 6a as a function of temperature and for different applied voltages. To proceed with our model we make use of two experimental observations:

First observation: In the experiments it was found that the forming process for resistive switching requires a critical applied voltage of about 5 V (see Figure S2a, Supporting Information). According to Figure 6a, this means that the maximum difference between the oxygen activities at the BE and at the TE would be about 300 orders of magnitude at a temperature of 300 K and about 100 orders of magnitude at 1000 K.

Second observation: In the experiments it was found that during the forming process at the BE a filament was formed that consists of the metallic, Ti-rich phase $\text{SrTi}_{11}\text{O}_{20}$ and is

accompanied by the RP phase $\text{Sr}_3\text{Ti}_2\text{O}_7$. The formation of these two phases can be described as a decomposition of highly non-stoichiometric STO at the BE, $\text{SrTiO}_{3-\delta(\text{BE})}$ with $\delta(\text{BE}) = 0.097$.



Here we assumed that no oxygen is lost during the decomposition.

Using literature data for the reduction of STO,^[20,54] we can estimate the oxygen activity at the BE, $aO_2(\text{BE})$, corresponding to $\delta(\text{BE}) = 0.097$. The results are shown in Figure 6b. It must be emphasized that Figure 6b shows the absolute value of the critical aO_2 that has to be reached at the BE to obtain a non-stoichiometry $\delta(\text{BE}) = 0.097$ in accordance with Equation (1), while Figure 6a depicts the maximum ratio of the oxygen activities at the BE and at the TE, $aO_2(\text{BE})/aO_2(\text{TE})$ corresponding to “full polarization”. Nevertheless the two results are compatible with each other and show that the oxygen activity within STO near the BE is extremely low.

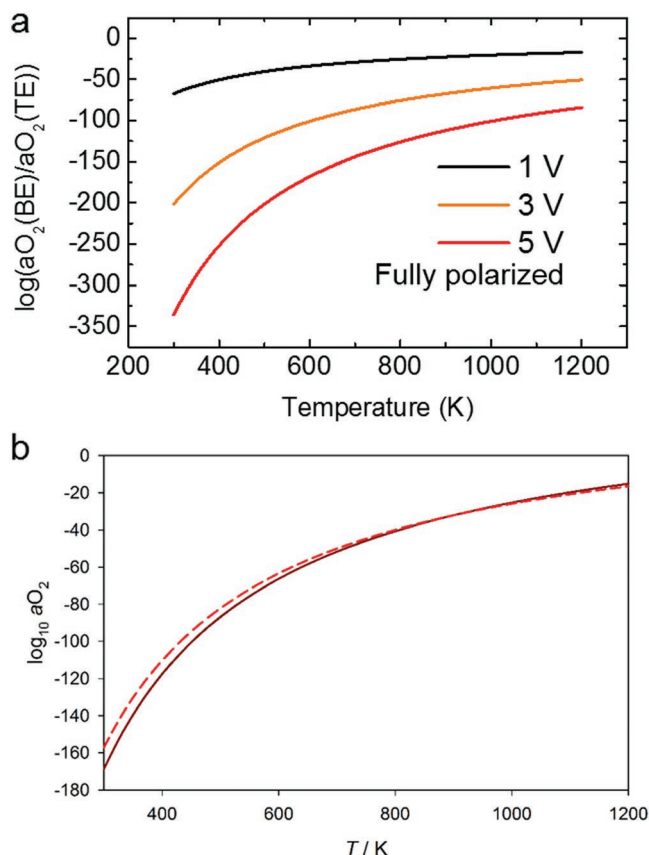


Figure 6. Calculated oxygen activity. a) Dependence of the ratio of the oxygen activities at the BE and at the TE, $a_{O_2}(BE)/a_{O_2}(TE)$ on temperature (in K) and applied voltage, assuming a fully polarized state (see the text). b) Critical oxygen activity a_{O_2} for which $\delta = 0.097$ in $SrTiO_{3-\delta}$ as a function of temperature T (values for the equilibrium constant K_{red} taken from Moos and Hardt^[20] solid line, and De Souza et al.^[54] dotted line).

Based on both the experimental findings and the above estimations, we propose a phase diagram for STO at very low oxygen activities, which is shown in Figure 7. According to Figure 7, STO is only stable above a critical oxygen activity $a_{O_2,decomp}$ corresponding to $\delta_{decomp} = 0.097$. Above this critical value Sr-rich STO can coexist with $Sr_3Ti_2O_7$ while Ti-rich STO can coexist with $SrTi_{11}O_{20}$. Below $a_{O_2,decomp}$ only the two phases $Sr_3Ti_2O_7$ and $SrTi_{11}O_{20}$ co-exist. (The critical oxygen activity $a_{O_2,decomp}$ could be temperature dependent.) The proposed decomposition of STO at a critical non-stoichiometry $\delta_{decomp} = 0.097$ is supported by atomistic calculations (with empirical pair potentials)^[55–57] of the reaction energy for the decomposition reaction in Equation (1). Depending on the empirical potentials that are used we obtain reaction energies ΔE between -0.8 and -2.4 eV showing that the decomposition is energetically very favorable.

Figure 8a shows schematically the a_{O_2} -profile across the STO film due to electrochemical polarization when the oxygen activity at the BE is still above the critical value $a_{O_2,decomp}$ and no decomposition of STO takes place. By increasing the applied voltage and lowering the oxygen activity at the BE below $a_{O_2,decomp}$, decomposition of STO takes place, and the metallic filament $SrTi_{11}O_{20}$ is formed together with the RP phase $Sr_3Ti_2O_7$. Now the oxygen activity profile is no longer 1D, but 3D as shown

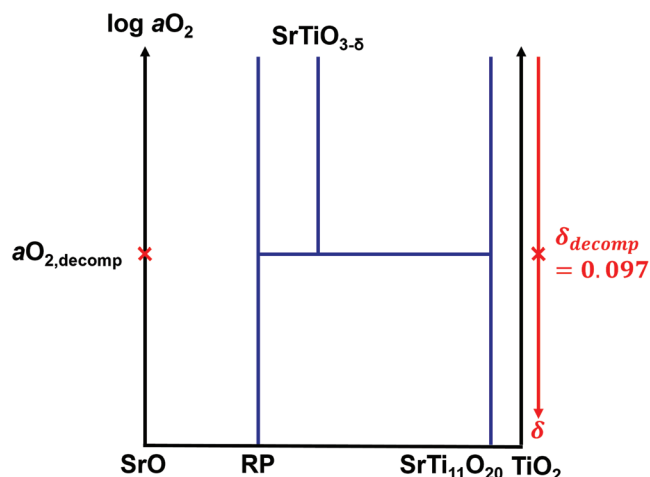
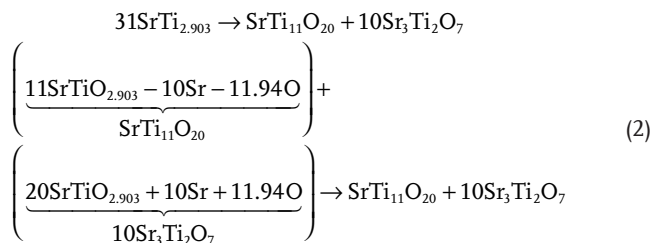


Figure 7. Schematic phase diagram of SrO - TiO_2 by oxygen activity. Proposed phase diagram of second kind for the system SrO - TiO_2 showing decomposition of STO to the RP-phase $Sr_3Ti_2O_7$ and the Ti-rich phase $SrTi_{11}O_{20}$ below the decomposition oxygen activity $a_{O_2,decomp}$. The temperature corresponds to the (unknown) temperature in the center of the SCL (see Figure 6c).

schematically by the contour plot in Figure 8b. At the tip of the filament three phases co-exist, $SrTiO_{2.903}$, $Sr_3Ti_2O_7$, and $SrTi_{11}O_{20}$. According to Gibbs' phase rule, for a three-phase equilibrium in a three-component system (Sr, Ti, and O), there are only two thermodynamic degrees of freedom left, which are the total pressure p and the temperature T . This means that the oxygen activity at the tip of the filament, $a_{O_2,decomp}$, is thermodynamically fixed. Once the applied voltage has surpassed the critical value corresponding to $a_{O_2,decomp}$ and the filament was formed, it will continue to grow towards the TE. The filament growth can thus be regarded as the motion of the thermodynamically fixed point $a_{O_2} = a_{O_2,decomp}$ from the BE towards the TE.

The kinetics of the filament growth depends on the transport of oxygen away from the tip of the filament (to establish the decomposition non-stoichiometry $\delta_{decomp} = 0.097$) and the reaction kinetics of the proper decomposition reaction in Equation (1) as well. Taking a closer look at the decomposition reaction in Equation (1) shows that it can be rewritten as follows:



Thus, decomposition of $SrTiO_{2.903}$ requires only the redistribution of strontium and oxygen corresponding to transport of both species near the filament tip from right to left (Figure 8c), i.e., perpendicular to the direction of oxygen (vacancy) motion due to the applied voltage. It is well known that in STO the diffusion coefficient of Sr-vacancies is much lower and has a much higher activation energy than the diffusion coefficient of O-vacancies (Figure 8d). Thus, we can conclude that: i) the rate

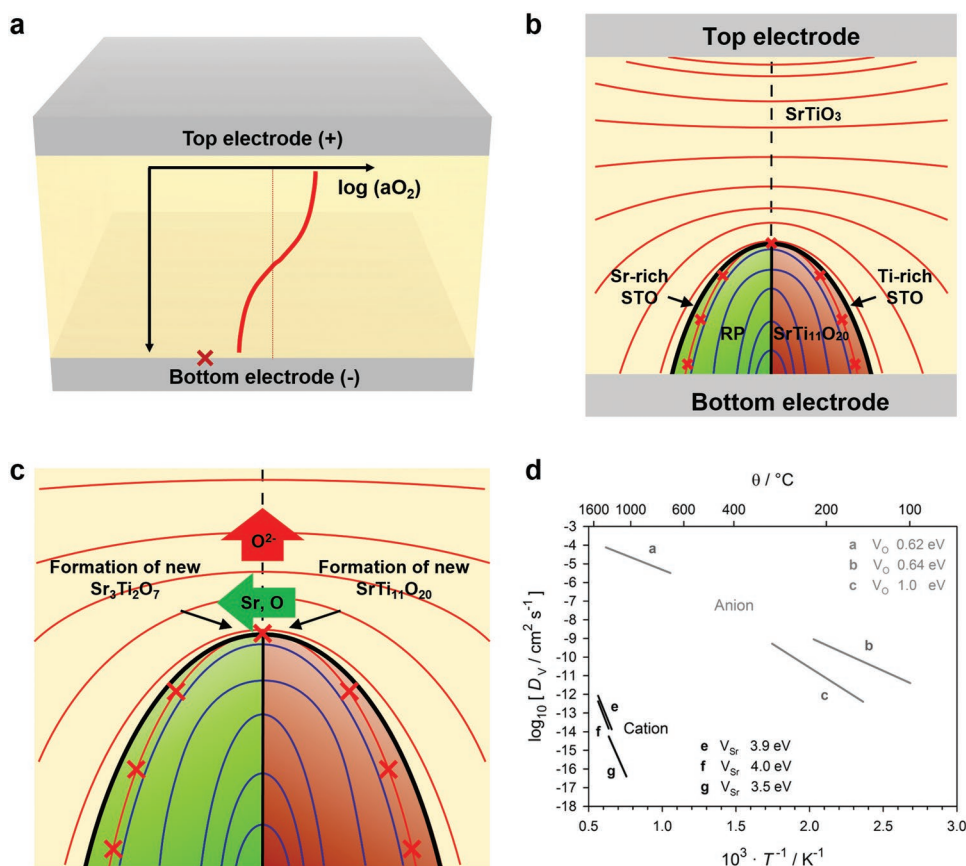


Figure 8. Filament formation through propagation of critical oxygen activity. Filament formation in STO near the BE due to electrochemical polarization. a) Oxygen activity profile (thick red line) across the STO film long within the SCL adjacent to the GB when the oxygen activity near the BE is still above the decomposition value (*). The red dashed line depicts the constant oxygen activity prior to polarization. b) Oxygen activity contour plot, when the oxygen activity near the BE is below the decomposition value and the filament $SrTi_{11}O_{20}$ and the RP phase $Sr_3Ti_2O_7$ have nucleated according to the decomposition reaction in Equation (1). The red and blue lines indicate equipotential surfaces with different oxygen activities: red lines 1 for $a_{O_2}^{\text{max}} = a_{O_2}^{\text{TE}}$, 2–9 for $a_{O_2}^* < a_{O_2} < a_{O_2}^{\text{max}}$; * for $a_{O_2} = a_{O_2}^*$ and blue lines 10–14 $a_{O_2}^{\text{BE}} < a_{O_2} < a_{O_2}^*$. c) Transport processes near the filament tip where the oxygen activity is fixed to $a_{O_2, \text{decomp}}$ (*). Oxygen ions are driven by the applied voltage towards the TE, preserving the critical non-stoichiometry δ_{decomp} for decomposition of STO. The components Sr and O are moving perpendicular to the motion of the oxygen ions from right to left, driven by the energy gain of the decomposition reaction in Equation (2). d) Vacancy diffusion coefficients in STO showing that Sr-vacancy diffusion is much slower than oxygen-vacancy diffusion and is the rate limiting step for filament growth. d) Adapted with permission.^[61] Copyright 2016, Wiley-VCH.

limiting step for the kinetics of filament growth is determined by the slow redistribution of Sr (vacancies) and ii) requires higher temperatures than the initial polarization process of oxygen (vacancies) due to the applied voltage.

In principle, the above model allows for decomposition of STO along the complete contact line of the GB and the BE, which would result in a “planar filament” that grows adjacent to the complete GB. However, the decomposition of STO according to Equation (2) requires nucleation of the two new phases $Sr_3Ti_2O_7$ and $SrTi_{11}O_{20}$. Once primary nuclei of the two new phases have formed at a certain position along the GB/BE contact line (see Figure 9) any secondary nuclei that form later will experience a smaller driving force for growth than the primary nuclei. The driving force for oxygen vacancies to the filament tip is $\Delta\eta(O^{2-})/\Delta x$, where $\Delta\eta(O^{2-})$ is the difference in electrochemical potentials of oxygen ions between the TE and the filament tip and Δx is the distance between these two positions. Regarding that $O^{2-} \leftrightarrow \frac{1}{2} O_2 + 2e^-$ and $\Delta\eta(O^{2-}) = \frac{1}{2} \Delta\mu(O_2) + 2\Delta\eta(e^-)$ shows that $\Delta\eta(O^{2-})$ consists of two parts, the first part,

$\Delta\mu(O_2) = \mu(O_2)_{\text{TE}} - \mu(O_2)_{\text{decomp}}$, is identical for both the primary and the secondary nucleus as both chemical potentials are thermodynamically fixed. The second part, $2\Delta\eta(e^-)$, is also identical as the Ti-rich filament, $SrTi_{11}O_{20}$, is metallic (see experimental results above) and the electrochemical potential of electrons drops completely within STO between the TE and the filament tip, resulting in $\Delta\eta(e^-) = -F \cdot V$, where V is the applied voltage. Thus, the only difference in the driving force $\Delta\eta(O^{2-})/\Delta x$ for growth of both nuclei is the distance Δx between TE and filament tip (see Figure 9). As $\Delta x_{\text{primary nucleus}}$ is smaller than $\Delta x_{\text{secondary nucleus}}$ the primary nucleus experiences a larger driving force than the secondary nucleus and will grow faster. This type of self-accelerated growth process or morphological instability is well known in other systems with moving boundaries.^[58,59] As a result of this mode-selection process, a single, truncated conical shape filament will form within the GB plane.

Figure 10 shows schematically the time evolution of the growth of the filament, corresponding to the growth of the primary nucleus in Figure 9. After nucleation (Figure 10a), the

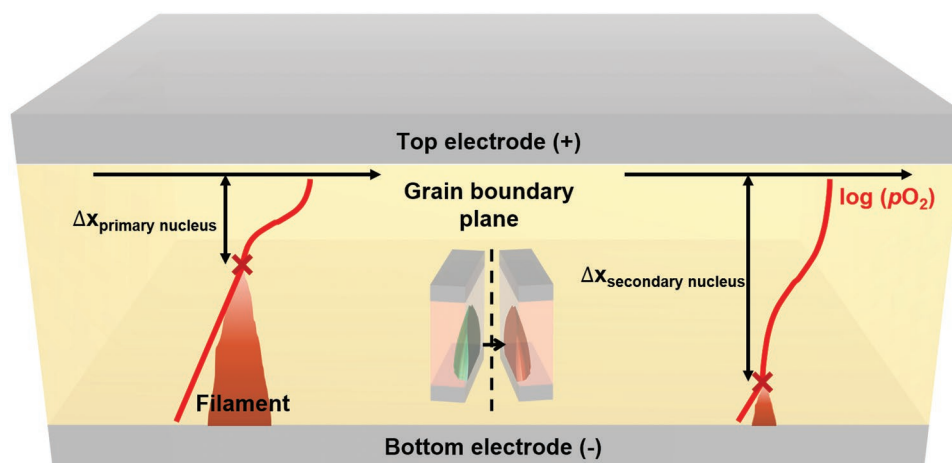


Figure 9. Cross-section of filament during the growth. Cross-section of the film showing the GB plane with a primary nucleus (filament) and a secondary nucleus. Because the GB plane separates the Sr-rich and the Ti-rich parts of the filament (see cross-section in Figure 8 which is perpendicular to the one shown here) only the Ti-rich part of the two new phases is shown. This part is metallic and the origin of the high conductivity of the filament. For simplification only a 1D-cut of the oxygen activity contour plot (see Figure 8b) is shown.

filament tip moves towards the TE driven by the applied voltage (Figure 10b). As the Ti-rich phase $\text{SrTi}_{11}\text{O}_{20}$ is metallic, the resistance of the film decreases during filament growth (even at constant applied voltage), enabling the transition from HRS to LRS. During the tip of the filament reaches the region near the TE (Figure 10c), there are two possible scenarios:

i) The applied voltage is decreased before the tip has connected to the TE. As the oxygen mobility in the filament may possibly be much lower than that in the STO near the GB because of lower symmetry, the thermodynamically fixed triple point where $a\text{O}_2 = a\text{O}_{2,\text{decomp}}$ will stay near the TE and the incomplete filament will be preserved. (Forming through multiple I - V sweeps). ii) The applied voltage is increased until the filament reaches the TE. Now BE and TE are connected by

the metallic filament (complete breakthrough) and I - V curve becomes ohmic. (SET)

For the RESET operation, due to the high resulting current there will be strong Joule heating, in particular in the regions where the filament has a small cross-section. Two scenarios are possible. iia) Joule heating leads to diffusion of ions such that Sr and O are redistributed from left to right, and STO will form again starting near the TE. iib) Joule heating enables reoxidation of the filament due to oxygen coming from the surrounding STO bulk. In both cases, there will be local rupture of the filament and the resistance will increase rather abruptly.

Finally, we consider what will happen if the external voltage is turned off resulting in a vanishing electric current and cooling down of the SCL region. Then, the field-driven flux of

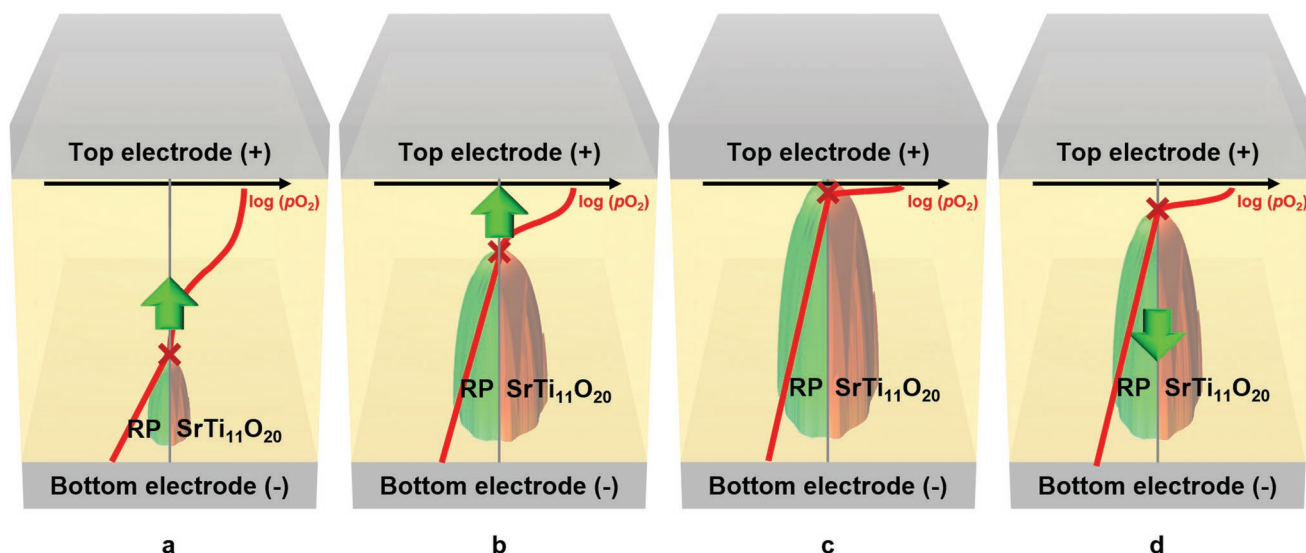


Figure 10. Time evolution of filament. a–c) Time evolution of the filament during increase of the applied voltage and d) after decrease of the applied voltage. a) Shortly after nucleation of the filament at the BE. b) Growth of the filament towards the TE. c) Filament nearly reaches the TE. d) Shrinkage of the filament after decreasing the applied voltage, keeping however the same polarity. For simplification only a 1D-cut of the oxygen activity contour plot (see Figure 8b) is shown.

oxygen ions also vanishes, and the still existing strong chemical polarization drives the oxygen ions back towards the BE. Due to the lower temperature the diffusivity of oxygen and its flux will be much lower than with applied voltage. More importantly, the filament, $\text{SrTi}_{11}\text{O}_{20}$, and the co-existing RP phase, $\text{Sr}_3\text{Ti}_2\text{O}_7$, are, however, still stable because dissolution of both phases requires redistribution of the components Sr and O. But at lower temperatures diffusion of Sr is orders of magnitude slower than oxygen diffusion due its higher activation energy (see Figure 8d). Thus, without external bias and the corresponding electric current and Joule heating the filament structure is kinetically stabilized, resulting in long endurance.

Using in situ I - V measurements and HRTEM images in combination with EELS, we have demonstrated that the filament structure in polycrystalline Pt/STO/Pt memory devices consists of a metallic, Ti-rich $\text{SrTi}_{11}\text{O}_{20}$ phase that is accompanied by the Sr-rich RP structure $\text{Sr}_3\text{Ti}_2\text{O}_7$. The $\text{SrTi}_{11}\text{O}_{20}$ phases were preferentially generated at GBs where a 90° twist in the $\{112\}$ plane occurred between STO (110) and (111) grains. Based on these experimental observations, we propose a new and detailed model for the reversible resistive switching in STO; electrochemical polarization by an applied voltage, the resulting oxygen redistribution and decomposition of highly non-stoichiometric $\text{SrTiO}_{2.903}$ into Ti-rich $\text{SrTi}_{11}\text{O}_{20}$ and Sr-rich $\text{Sr}_3\text{Ti}_2\text{O}_7$ are responsible for the structural and related electrical transition between insulating and metallic phases. Filament rupture was evidently caused by high temperatures resulting from the large localized current density. Following rupture, the filaments were transformed back into STO. Without external bias, resulting in vanishing electric current and Joule heating the filament structure is kinetically stabilized due to the low diffusivity of Sr at room temperature.

Experimental Section

Film Growth: Polycrystalline STO films 50-nm thick were grown using pulsed laser deposition onto Pt-coated Si substrates (where the layer sequence of the substrate was Pt (100 nm)/Ti (≈ 10 nm)/ SiO_2 /Si). The 100-nm-thick Pt TE was then deposited using sputtering and patterned to form $25\ \mu\text{m}^2$. Details of the growth conditions and electrical properties of this Pt/STO/Pt system have been previously reported.^[35,36]

TEM Sample Preparation: TEM samples were prepared using FIB followed by a Nanomill. The sample modulation was carefully estimated and removed by the milling effect. The FIB sample preparation procedure is well established, and because of the success of modern FIB with low-energy ion beams (<2 kV), damage to the sample is limited. Furthermore, a Nanomill is employed, which is a focused low-energy Ar-ion miller from Fischione,^[60] to completely remove the remainder of the damaged layer at the surface of the specimens and successfully acquired clear EELS signals from the samples.

In Situ FORMING (or SET) and RESET Processes: An in situ STM/TEM double tilt holder (Nanofactory) was employed for the electrical switching and measurements. In situ FORMING (or SET) and RESET processes were both carried out using an STM tip in contact with the TE. Both procedures were sensitive to heating because of the vacuum environment (see Supporting Information). Thus, extensive and careful management of heat during the I - V measurements was required. The in situ FORMING process was achieved when a high voltage (<6 V) was applied. A current in the TEM specimens of $>30\ \mu\text{A}$ was prerequisite for the in situ FORMING or SET processes. To control the heating of the specimens, the in situ FORMING and RESET processes were carried out with a compliance current. In situ rupture of the filaments was achieved at currents >1 mA.

Filament Probing and Analysis: Filaments were identified via in situ probing and the results of both ex situ and in situ measurements were consistent. To probe the conducting channels underneath the insulating STO matrix, a Pt/Ir-coated W tip was in contact with the oxide film and scanned over the region of interest to probe for filaments. The Pt/Ir-coated W tip was used because of its large conductivity, inertness, and good sharpness. A pure W tip was not used (even though it was sharper than the Pt/Ir-coated tip) because the surface was more readily oxidized when in contact with the oxide films. Notably, the measured currents depended strongly on the properties of the STM tip, including their geometry and conductivity. Filaments were located on the basis of the local current. Following probing for filaments, HRTEM images and EELS analyses were carried out at the corresponding locations to investigate the crystal structure and electronic structure, respectively. The HRTEM images were further analyzed to investigate the orientation relationship between the filaments and neighboring matrix, which is indicative of filament nucleation. These experiments were carried out using a Philips F20 TEM equipped with Gatan image filter.

Supporting Information

Supporting Information is available from the Wiley Online Library or from the author.

Acknowledgements

This work was supported by IBS-R009-D1 through the Research Center Program of the Institute for Basic Science and by Basic Science Research Programs (NRF-2017R1A2B3011629), Engineering Research Center Program (NRF-2015R1A5A1037627), Creative Materials Discovery Program through the National Research Foundation of Korea (NRF-2017M3D1A1040688), and the German Research Foundation (DFG) through the collaborative research center, SFB 917 "Nanoswitches", at RWTH Aachen University.

Note: The figures were reset in higher resolution on July 7, 2019, after initial publication online.

Conflict of Interest

The authors declare no conflict of interest.

Keywords

memristors, nanofilaments, resistive switching, transmission electron microscopy (TEM)

Received: February 27, 2019
Published online: May 20, 2019

- [1] R. Waser, M. Aono, *Nat. Mater.* **2007**, 6, 833.
- [2] R. Waser, R. Dittmann, G. Staikov, K. Szot, *Adv. Mater.* **2009**, 21, 2632.
- [3] A. Sawa, *Mater. Today* **2008**, 11, 28.
- [4] J. J. Yang, D. B. Strukov, D. R. Stewart, *Nat. Nanotechnol.* **2013**, 8, 13.
- [5] D. B. Strukov, G. S. Snider, D. R. Stewart, R. S. Williams, *Nature* **2008**, 453, 80.
- [6] J. Borghetti, G. S. Snider, P. J. Kuekes, J. J. Yang, D. R. Stewart, R. S. Williams, *Nature* **2010**, 464, 873.
- [7] Y. Aoki, C. Wiemann, V. Feyer, H.-S. Kim, C. M. Schneider, H. Ill-Yoo, M. Martin, *Nat. Commun.* **2014**, 5, 3473.
- [8] C. Kura, Y. Aoki, E. Tsuji, H. Habazaki, M. Martin, *RSC Adv.* **2016**, 6, 8964.
- [9] D.-H. Kwon, K. M. Kim, J. H. Jang, J. M. Jeon, M. H. Lee, G. H. Kim, X.-S. Li, G.-S. Park, B. Lee, S. Han, M. Kim, C. S. Hwang, *Nat. Nanotechnol.* **2010**, 5, 148.

- [10] J.-Y. Chen, C.-L. Hsin, C.-W. Huang, C.-H. Chiu, Y.-T. Huang, S.-J. Lin, W.-W. Wu, L.-J. Chen, *Nano Lett.* **2013**, 13, 3671.
- [11] X. Guo, C. Schindler, S. Menzel, R. Waser, *Appl. Phys. Lett.* **2007**, 91, 133513.
- [12] R. Yasuhara, K. Fujiwara, K. Horiba, H. Kumigashira, M. Kotsugi, M. Oshima, H. Takagi, *Appl. Phys. Lett.* **2009**, 95, 012110.
- [13] Y. Yang, P. Gao, S. Gaba, T. Chang, X. Pan, W. Lu, *Nat. Commun.* **2012**, 3, 732.
- [14] Q. Liu, J. Sun, H. Lv, S. Long, K. Yin, N. Wan, Y. Li, L. Sun, M. Liu, *Adv. Mater.* **2012**, 24, 1844.
- [15] M. Kudo, M. Arita, Y. Ohno, Y. Takahashi, *Appl. Phys. Lett.* **2014**, 105, 173504.
- [16] U. Celano, L. Goux, R. Degraeve, A. Fantini, O. Richard, H. Bender, M. Jurczak, W. Vandervorst, *Nano Lett.* **2015**, 15, 7970.
- [17] J. F. Schooley, W. R. Hosler, M. L. Cohen, *Phys. Rev. Lett.* **1964**, 12, 474.
- [18] J. Mannhart, D. G. Schlom, *Science* **2010**, 327, 1607.
- [19] I. Denk, F. Noll, J. Maier, *J. Am. Ceram. Soc.* **1997**, 80, 279.
- [20] R. Moos, K. H. Hardtl, *J. Am. Ceram. Soc.* **1997**, 80, 2549.
- [21] R. A. De Souza, *Adv. Funct. Mater.* **2015**, 25, 6326.
- [22] T. Shi, Y. Chen, X. Guo, *Prog. Mater. Sci.* **2016**, 80, 77.
- [23] R. Merkle, J. Maier, *Angew. Chem., Int. Ed.* **2008**, 47, 3874.
- [24] N. G. Eror, U. Balachandran, *J. Solid State Chem.* **1981**, 40, 85.
- [25] R. Moos, T. Bischoff, W. Menesklou, K. H. Hardtl, *J. Mater. Sci.* **1997**, 32, 4247.
- [26] Z. Xu, Y. Bando, W. Wang, X. Bai, D. Golberg, *ACS Nano* **2010**, 4, 2515.
- [27] T. Fujii, M. Arita, Y. Takahashi, I. Fujiwara, *Appl. Phys. Lett.* **2011**, 98, 212104.
- [28] S.-J. Choi, G.-S. Park, K.-H. Kim, S. Cho, W.-Y. Yang, X.-S. Li, J.-H. Moon, K.-J. Lee, K. Kim, *Adv. Mater.* **2011**, 23, 3272.
- [29] Y. Yang, P. Gao, L. Li, X. Pan, S. Tappertzhofen, S. Choi, R. Waser, I. Valov, W. D. Lu, *Nat. Commun.* **2014**, 5, 2382.
- [30] P. Gao, Z. Kang, W. Fu, W. Wang, X. Bai, E. Wang, *J. Am. Chem. Soc.* **2010**, 132, 4197.
- [31] G.-S. Park, Y.-B. Kim, S. Y. Park, X.-S. Li, S. Heo, M.-J. Lee, M. Chang, J.-H. Kwon, M. Kim, U.-I. Chung, R. Dittmann, R. Waser, K. Kim, *Nat. Commun.* **2013**, 4, 2382.
- [32] J. Kwon, A. A. Sharma, J. A. Bain, Y. N. Picard, M. Skowronski, *Adv. Funct. Mater.* **2015**, 25, 2876.
- [33] D. Cooper, C. Baeumer, N. Bernier, A. Marchewka, C. La Torre, R. E. Dunin-Borkowski, S. Menzel, R. Waser, R. Dittmann, *Adv. Mater.* **2017**, 29, 1700212.
- [34] B. Hessen, S. A. Sunshine, T. Siegrist, *J. Solid State Chem.* **1991**, 94, 306.
- [35] S. Lee, H. K. Yoo, S. H. Chang, L. G. Gao, B. S. Kang, M. J. Lee, C. J. Kim, T. W. Noh, *Appl. Phys. Lett.* **2011**, 98, 053503.
- [36] S. Lee, D.-H. Kwon, K. Kim, H. K. Yoo, S. Sinn, M. Kim, B. Kahng, B. S. Kang, *J. Phys. D: Appl. Phys.* **2012**, 45, 255101.
- [37] J. Schmachtel, H. Muller-Buschbaum, *Z. Naturfor. Teil B Anorg. Chem., Org. Chem.* **1980**, 35b, 4.
- [38] D. A. Muller, N. Nakagawa, A. Ohtomo, J. L. Grazul, H. Y. Hwang, *Nature* **2004**, 430, 657.
- [39] R. Egerton, *Electron Energy-Loss Spectroscopy in the Electron Microscope*, Springer Science & Business Media, New York **2011**.
- [40] Z. Zhang, W. Sigle, M. Rühle, *Phys. Rev. B* **2002**, 66, 094108.
- [41] M. Kim, G. Duscher, N. Browning, K. Sohlberg, S. Pantelides, S. Pennycook, *Phys. Rev. Lett.* **2001**, 86, 4056.
- [42] D.-H. Kwon, *Unraveling the Mechanism of Unipolar Resistive Switching in Transition Metal Oxides by Transmission Electron Microscopy*, Seoul National Univ. Press, Seoul, Republic of Korea **2015**.
- [43] W. Lee, S. Yoo, K. J. Yoon, I. W. Yeu, H. J. Chang, J.-H. Choi, S. Hoffmann-Eifert, R. Waser, C. S. Hwang, *Sci. Rep.* **2016**, 6, 20550.
- [44] P. R. Mickel, A. J. Lohn, C. D. James, M. J. Marinella, *Adv. Mater.* **2014**, 26, 4486.
- [45] G. Panomsuwan, O. Takai, N. Saito, *Solid State Commun.* **2013**, 158, 65.
- [46] K. Szot, W. Speier, G. Bihlmayer, R. Waser, *Nat. Mater.* **2006**, 5, 312.
- [47] K. Szot, G. Bihlmayer, W. Speier, *Solid State Phys.—Adv. Res. Appl.* **2014**, 65, 353.
- [48] S. Stille, C. Lenser, R. Dittmann, A. Koehl, I. Krug, R. Muenstermann, J. Perlich, C. M. Schneider, U. Klemradt, R. Waser, *Appl. Phys. Lett.* **2012**, 100, 223503.
- [49] S. P. Waldow, R. A. De Souza, *ACS Appl. Mater. Interfaces* **2016**, 8, 12246.
- [50] S. Nuansaeng, M. Yashima, M. Matsuka, T. Ishihara, *Chem.—Eur. J.* **2011**, 17, 11324.
- [51] D. B. Strukov, F. Alibart, R. Stanley Williams, *Appl. Phys. A* **2012**, 107, 509.
- [52] R. A. De Souza, *Phys. Chem. Chem. Phys.* **2009**, 11, 9939.
- [53] R. A. De Souza, V. Metlenko, D. Park, T. E. Weirich, *Phys. Rev. B* **2012**, 85, 218.
- [54] R. A. De Souza, F. Gunkel, S. Hoffmann-Eifert, R. Dittmann, *Phys. Rev. B* **2014**, 89, 241401.
- [55] K. R. Udayakumar, A. N. Cormack, *J. Phys. Chem. Solids* **1989**, 50, 55.
- [56] G. V. Lewis, C. R. A. Catlow, *J. Phys. C: Solid State Phys.* **1985**, 18, 1149.
- [57] A. Pedone, G. Malavasi, M. C. Menziani, A. N. Cormack, U. Segre, *J. Phys. Chem. B* **2006**, 110, 11780.
- [58] J. S. Langer, *Rev. Mod. Phys.* **1980**, 52, 1.
- [59] M. Martin, H. Schmalzried, *Berichte der Bunsengesellschaft für Phys. Chem.* **1985**, 89, 124.
- [60] R. R. Cerchiara, P. E. Fischione, J. Liu, J. M. Matesa, A. C. Robins, H. L. Fraser, A. Genc, *Micros. Today* **2011**, 19, 16.
- [61] R. A. De Souza, in *Resistive Switching* (Eds: D. Ielmini, R. Waser), Wiley-VCH, Weinheim, Germany **2016**, pp. 125–164.